Supplementary Information for

Imaging nanoscale photocarrier traps in solar water-splitting catalysts

Levi D. Palmer,[1] Wonseok Lee,[1] Pushp Raj Prasad,[2] Bradley W. Layne,[2] Han-Hsuan Wu,[3] Zejie Chen,[2] Jianguo Wen,[4] Yuzi Liu,[4] Xiaoqing Pan,[3,5,6] A. Alec Talin,[7] Akihiko Kudo,[8] Shane Ardo,[2,6,9] Joseph P. Patterson,[2,6] Thomas E. Gage,[4*] Scott K. Cushing[1*]

Corresponding authors. Email: scushing@caltech.edu (S.K.C.), tgage@anl.gov (T.E.G.)

This file includes:

Supplementary Text

Supplementary Figures 1 to 13

Supplementary Tables 1 to 2

Legends for Supplementary Videos 1 to 6

Other Supplementary Materials for this manuscript include the following:

Supplementary Videos 1 to 6

Supplementary Text

Zero-loss peak alignment

The zero-loss peak was aligned using a center-of-mass fit over a 150 pixel window centered at the highest amplitude of the low-loss spectrum. The low-loss and high-loss spectra are both corrected for the ZLP energy for each pixel with a 7 eV spectral shift applied to the high-loss spectrum according to the set drift tube voltage for dualEELS.

Atomic STEM iDPC image analysis

Atomic resolution iDPC images were acquired using a Thermo Fisher Panther segmented detector. The nanoparticle is aligned along the [110] zone axis using a double-tilt holder and the auto-tilt Velox feature when resolving the Kikuchi pattern. However, post-collection analysis of the iDPC image illustrates subtle off-zone axis tilt due to misalignment of the measured lattice parameters and atomic spacing compared to bulk $SrTiO_3$. As mentioned in the main text, we map the Sr and Ti atomic columns by identifying circular atomic features via template matching and fit their position with a 2D Gaussian profile. We analyze the fit positions to calculate the interatomic distances between Ti–Ti / Sr–Sr and Sr–Ti (main text Fig. 2E). The measured interatomic distances are corrected uniformly such that measured interatomic distances in the $SrTiO_3$ nanoparticle bulk match the reported crystallographic bond lengths. This is performed by rescaling the crystallographic distances such that the ideal long bond (Ti–Ti / Sr–Sr) matches the observed long bond in the bulk by $\cos(\Delta\theta)$, a factor equivalent to the averaged measured distance divided by the crystallographic bond distance. The entire map of fit atomic positions, along with the analyzed region and the acquired iDPC image, are shown in Extended Data Fig. 4.

Automatic Gatan spatial drift correction

Specimen drift was corrected using Gatan's automated live spatial drift correction. This built-in feature corrects for drift by adjusting the beam deflectors based on a cross-correlation image over a reference region. The cross-correlation quantifies the drift and an offset to the beam scan coordinates is applied. For the photomodulated and temperature-dependent STEM-EELS measurements in this study, drift is corrected once every row of the image, or every 62 pixels. Without drift correction enabled, the photomodulated STEM scan would have otherwise moved ~6 nm. This drift relates to ~0.2 nm drift per row or ~0.1% of each pixel on average between drift-corrected measurements.

Laser alignment procedure

Laser alignment onto the electron beam's optical axis requires a multi-stage process. First, IDES performs initial alignment of the laser and optics with the tool at atmosphere, which is typically performed during the tool's initial installation. Next, sub-millimeter alignment precision is achieved using the IDES optical alignment holder within the STEM side-entry port with the microscope under vacuum. Next, a series of low-to-high magnification alignment stages are performed to progressively increase the alignment precision to ~100 micrometer accuracy. This is achieved by using the laser to burn a hole in an amorphous carbon foil. Finally, the beam shift is corrected between low- and high-magnification imaging modes to ensure that the electron beam does not drift away from the laser spot aligned on the specimen.

Beam current stability and background subtraction

The beam current of the microscope is variable due to oxidation of the cold field-emission gun, influenced by its vacuum quality. To refresh the current, either a high-temperature or low-temperature flash is performed. The tip was typically low-T flashed prior to the laser power or temperature hysteresis cycles. The estimated beam current was ~170 pA at the specimen.

Additionally, the variable background induced by spatial and beam-current-dependent fluctuations of the zero-loss peak was removed using a power-law fit. The subtracted fit backgrounds of the image-averaged data are shown in Supplementary Fig. 5.

Irradiance (power density) calculations

The laser irradiance is calibrated according to the set laser power and appreciable losses due to the fiber-coupled housing and optics used for coupling into the STEM.

Photomodulated STEM-EELS analysis and rigid shift model

All STEM-EELS data was analyzed using the HyperSpy Python loader; analysis scripts and data are available online[58].

Spatially resolved maps were generated from energy-aligned low-loss EELS spectrum images, where the ZLP in each pixel of each spectrum image was fit using center-of-mass analysis and aligned to 0 eV. Spectrum images were acquired under pump-off and pump-on conditions. The ZLP-aligned datasets have dimensions corresponding to pump condition, spatial row, spatial column, and energy loss. For each spatial pixel, spectra from repeated pump-off measurements were averaged using the indices corresponding to 0 mW excitation, while spectra from repeated pump-on measurements were averaged using the indices corresponding to 300 mW excitation (results for all pump-on conditions are shown in the supporting movies).

At each pixel, the pump-off and pump-on spectra were first normalized to the maximum spectral intensity within the 13–17 eV energy-loss window, which corresponds to the primary plasmon for photocarrier excitations. This normalization was applied to reduce the influence of pixel-to-pixel intensity variations of the probe's descan alignment and to correct for differences in total signal level between spectra. A logarithmic differential spectrum was then calculated as:

$$\Delta(E) = ln\left(\frac{I_{300}(E) + \epsilon}{I_0(E) + \epsilon}\right) \times 1000$$

where $I_{300}(E)$ and $I_0(E)$ are the normalized pump-on and pump-off spectra, respectively, and ε = 10^{-10} was added to avoid division by zero. The differential spectrum was smoothed using a Savitzky–Golay filter with a 61-point window and third-order polynomial. The spectrum was then baseline-offset by subtracting the value of the differential spectrum at the largest plasmon peak's tail at approximately 33 eV, forcing the tail of its differential response to be aligned to zero at 33 eV. The same normalized differential spectrum was used to generate the initial EM-field and heating maps, but the maps were obtained by integrating over different energy-loss windows.

EM-field map. The EM-field map represents the spatial distribution of the pump-induced low-energy response outside the nanoparticle and is interpreted here as the EM-field-related response. This map was generated by integrating the smoothed pump-on minus pump-off differential spectrum over the 11–15 eV energy-loss range:

$$M_{\mathrm{EM}(i,j)} = \sum_{E=11-15\mathrm{eV}} \Delta(E,i,j)$$

where $M_{\mathrm{EM}(i,j)}$ is the integrated EM-field response at spatial pixel (*i,j*). This integration window captures the low-loss spectral region where the pump-induced optical/electromagnetic response is most apparent in the initial differential spectrum.

Heating map. A separate heating map was generated from the higher-energy region of the same differential low-loss spectra. For each pixel, the differential signal was integrated over the 31.5–33 eV energy-loss window:

$$M_{\mathrm{heat}(i,j)} = \sum_{E=31.5-33\mathrm{eV}} \Delta(E,i,j)$$

This higher-energy integration window was selected to track spectral changes associated with pump-induced heating corresponding to the most intense, higher-energy plasmon peak. After the heating map was generated, outlier pixels beyond two standard deviations of the image average were set to zero amplitude on the map. Nonzero values in the temperature map were used to calculate the mean and standard deviation of the nanoparticle's differential temperature. The differential was calibrated using the differential amplitude in the 31.5–33 eV energy-loss region from the resistive heating control experiments.

EM- and heat-corrected carrier map. Analysis was then performed to isolate the carrier-related spectral response after accounting for[1] beam-induced field and[2] thermal effects. This correction was necessary for two respective reasons.[1] The electron beam current induced visible fluctuations of the EM field background signal stemming as tails off the ZLP.[2] Pump-induced heating also shifted the low-loss peak at 13–17 eV. If not removed, these amplitude- and shift-induced differential features overlapped and obscured differential plasmon features used to quantify carrier-related signal.

For each pixel, the pump-off spectrum was again obtained by averaging the 0 mW spectra, and the high-power spectrum was obtained by averaging the 300 mW spectra. Both spectra were again normalized to their maximum intensity in the 13–17 eV range, and the differential spectrum was calculated as above. Each raw differential spectrum was again offset so the largest plasmon's tail at 33 eV was zero. To account for EM-field contributions of the fluctuating ZLP tail, a power-law background of the form:

$$B(E) = aE^b$$

was then fit over the 2–45 eV range and subtracted from the raw differential spectrum. The fit power-law background-subtracted differential spectrum was smoothed using a Savitzky–Golay filter with a 41-point window and third-order polynomial.

To model the thermal contribution, the normalized 300 mW spectrum was shifted rigidly along the energy axis by integer pixel offsets ranging from −6 to +6 pixels. For each tested shift, the shifted high-power spectrum was compared to the unshifted pump-off spectrum by calculating a simulated shift-induced differential spectrum:

$$\Delta_{shift}(E, d) = ln\left(\frac{I_{300}^{norm}(E + d)}{I_{0}^{norm}(E)}\right)$$

where *d* is the tested integer-pixel energy shift to correct for thermal effects. Each simulated shift-induced differential spectrum was also offset to zero at 33 eV. The shift that best reproduced the measured differential spectrum was identified by minimizing the summed squared residual between the measured background-subtracted differential spectrum and the simulated shift-induced differential spectrum over the 4–33 eV fitting window:

$$\chi^2(d) = \sum_{E=4-33\text{eV}} \left[\Delta_{bg}(E) - \Delta_{shift}(E, d)\right]^2$$

where $\Delta_{bg}(E)$ is the measured differential spectrum after the first power-law background subtraction. This fitting procedure determines, independently for every pixel, the rigid spectral shift that most closely accounts for the observed pump-induced differential response over the broad low-loss energy range.

The best-fitting rigid-shift differential spectrum was then subtracted from the measured background-subtracted differential spectrum:

$$\Delta_{clean}(E) = \Delta_{bg}(E) - \Delta_{shift}(E, d_{best})$$

This subtraction removes the component of the pump-induced differential signal that can be explained by a thermal redshift of the spectrum. In other words, this subtraction accounts for the spectral redshifts from thermal expansion that are typically measured using plasmon energy expansion thermometry. Importantly, the correction is performed at each pixel independently, allowing the magnitude and direction of the thermal shift to vary spatially across the spectrum image. Ideally, the heating control STEM-EELS datasets could be used for this purpose, but the spatial drift created by the resistive heating holder was too significant.

After subtracting the best-fit shift contribution, a second power-law background subtraction was applied over the 2–45 eV range. This second background subtraction removes any residual slope or slowly varying baseline introduced by the rigid-shift correction. The resulting corrected spectrum, $\Delta_{corr}(E)$, represents the residual pump-induced response after removal of the broad thermal-shift contribution and background.

The final thermally corrected carrier map was generated by integrating the negative of this corrected residual differential spectrum over the 12–16 eV energy-loss window:

$$M_{\mathrm{carrier}(i,j)} = \sum_{E=12-16\mathrm{eV}} -\Delta_{corr}(E,i,j)$$

Because the 300 mW spectra were rigid-shifted, instead of the non-photomodulated 0 mW spectra, a negative sign was applied to the spectra so negative-going residual differential features in the 12–16 eV range appear as positive carrier-map intensity.

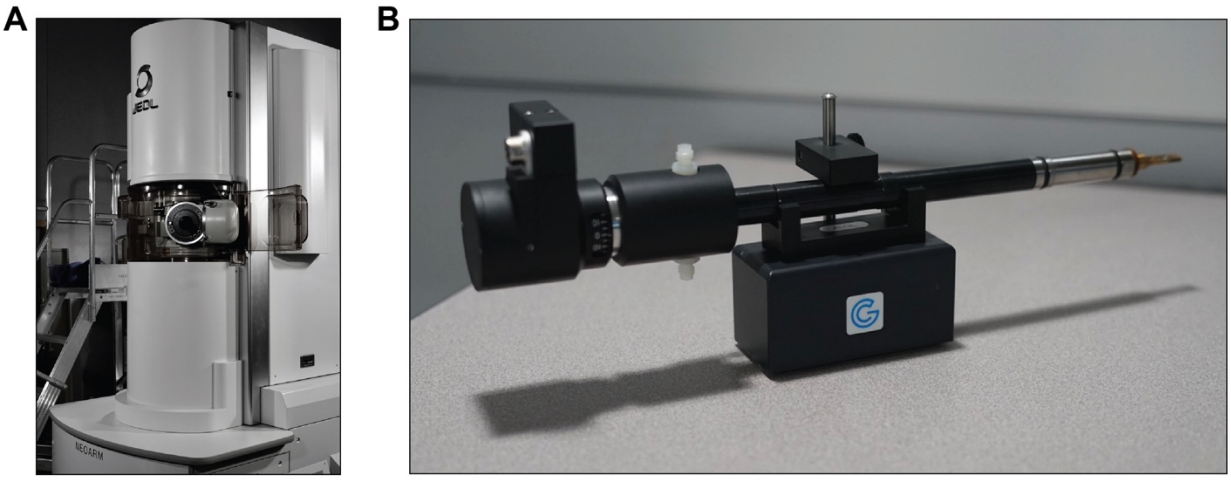

Supplementary Fig. 1 | Photomodulated STEM-EELS platform with in situ heating. (**A**) The JEOL NEOARM microscope with optically coupled photoexcitation through the integrated IDES laser module. (**B**) The in situ bulk heating holder allows temperature-dependent control measurements through side-entry specimen insertion.

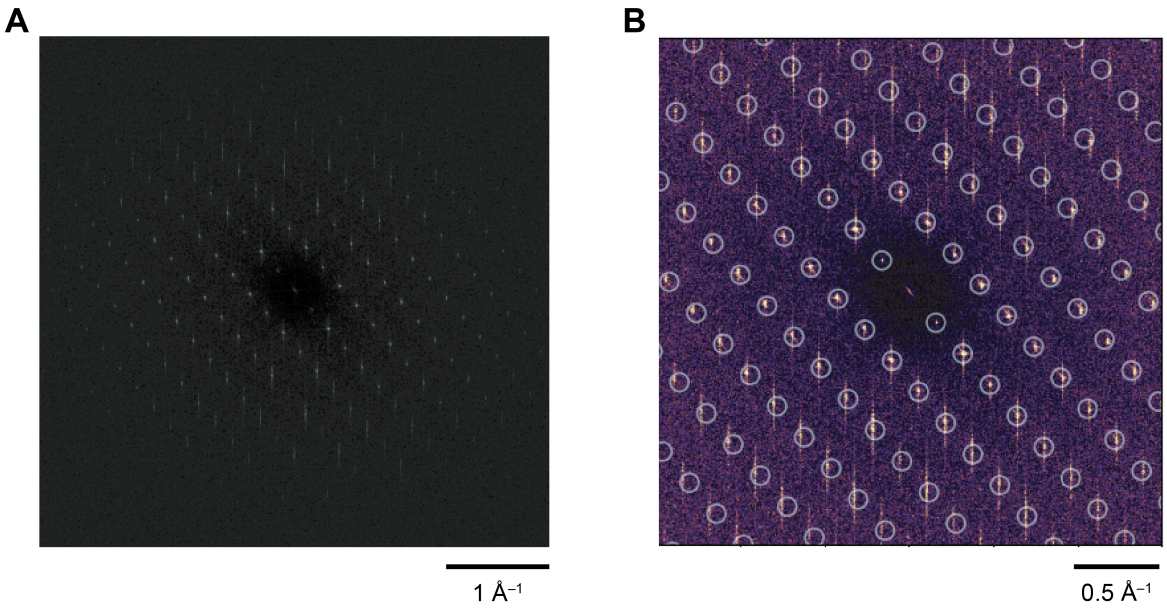

Supplementary Fig. 2 | Fourier transform of atomic position map. (**A**) The virtual diffraction pattern of the atomic resolution imaging in Extended Data Fig. 4B. (**B**) The virtual diffraction pattern color-scaled for visibility and the simulated [110] diffraction pattern of $SrTiO_3$ overlaid in white circles.

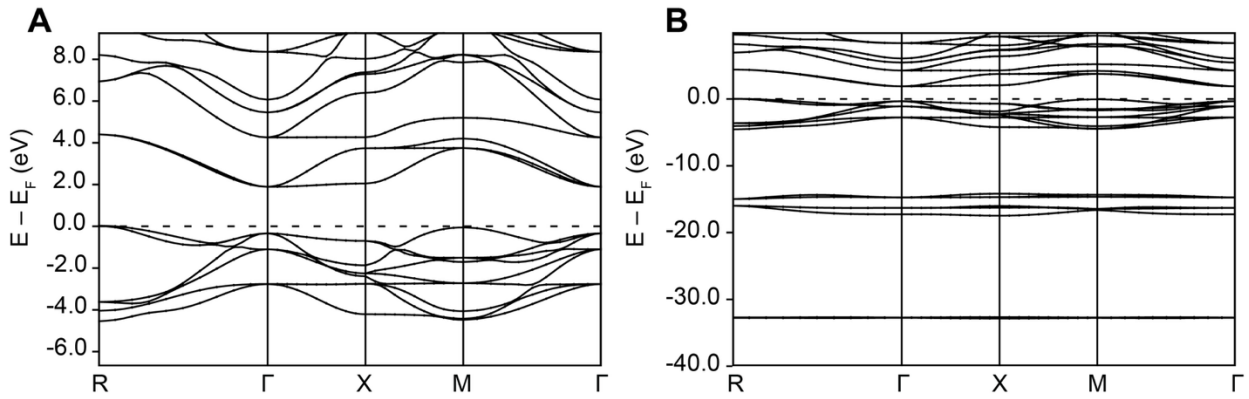

Supplementary Fig. 3 | $SrTiO_3$ band structure. The DFT-calculated band structure of undoped, bulk strontium titanate to better visualize (**A**) the valence states and (**B**) the valence and core states as compared to main text Fig. 3.

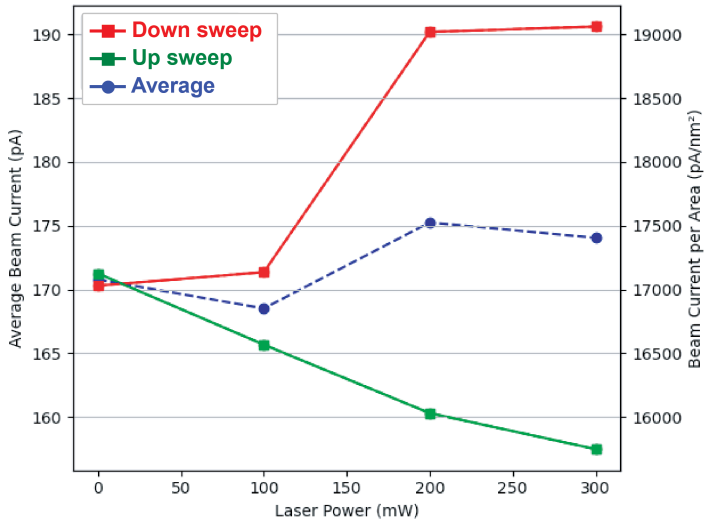

Supplementary Fig. 4 | Photomodulated STEM-EELS beam current. Approximate beam current values were recorded for the up and down sweeps as a function of laser power laser power. This approximate beam current was measured using the total counts in each EEL spectrum acquired using the direct electron detector with an additional factor of 25 considered for lost counts due to detector-blocked electrons and high-loss scattering. A 0.25 s × 0.07% live time is considered as the acquisition time with a 1 Å probe size.

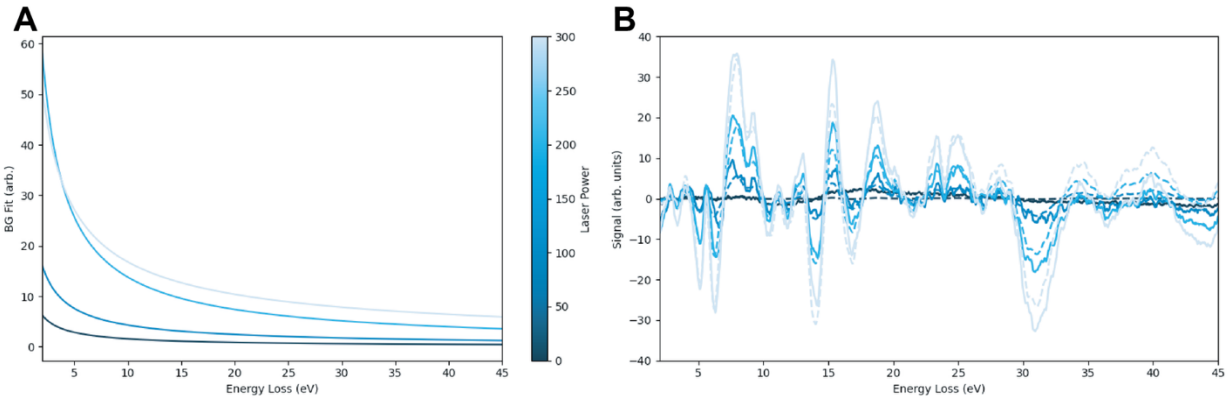

Supplementary Fig. 5 | Background fitting for average photomodulated STEM-EELS datasets. (**A**) The power-low fitting used to model the fluctuations in the zero-loss peak induced locally by EM field as well as the change in beam current. (**B**) Spectrally fitting the photothermal heating background from the STEM-EELS image-averaged and temperature-dependent dataset to the four average photomodulated STEM-EELS image-averaged datasets. The fittings are uniformly scaled by a factor as shown in (B), and the fit is directly subtracted from these datasets to produce main text Fig. 4C.

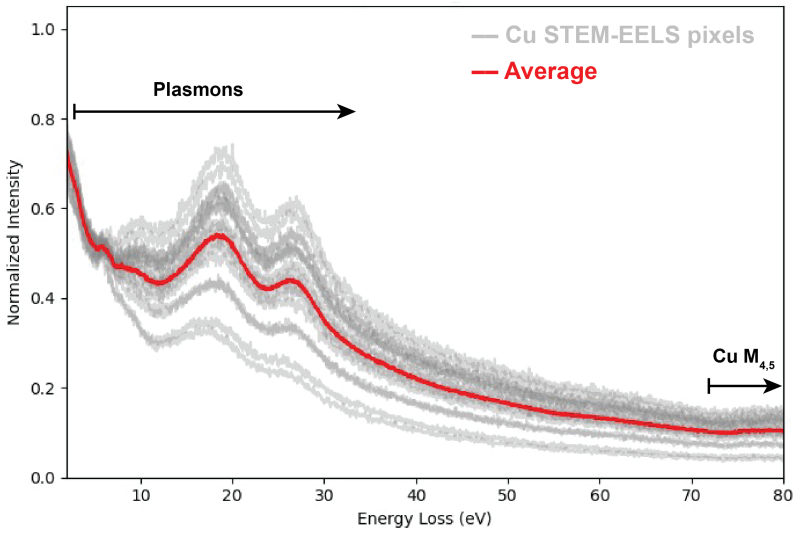

Supplementary Fig. 6 | STEM-EELS spectra of the Cu nanoparticle's volume plasmon and $M_{4,5}$ edge. Binning the photomodulated low-loss spectra over the largest Cu nanoparticle's region of interest (shown in Extended Data Fig. 1C) depicts the ability to resolve the Cu plasmon peaks.

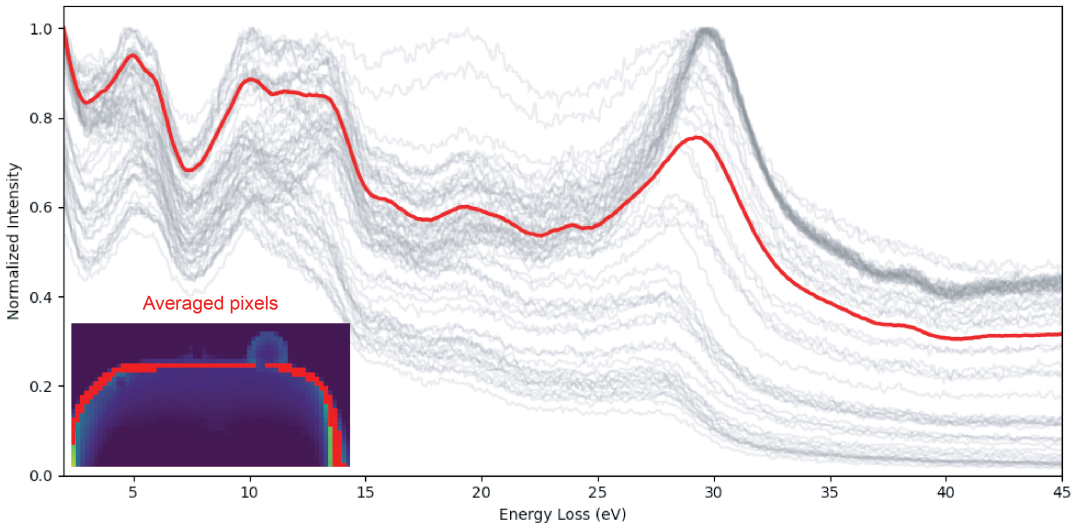

Supplementary Fig. 7 | STEM-EELS spectra over the surface oxygen vacancy regions. STEM-EELS pixels are averaged over the outer region of the nanoparticle where the oxygen vacancies are localized. The volume plasmon peaks redshift due to the lower carrier density of the disordered oxygen vacancy phase. The inset depicts the surface plasmon intensity STEM-EELS map (3–8 eV) with the pixels averaged highlighted in red.

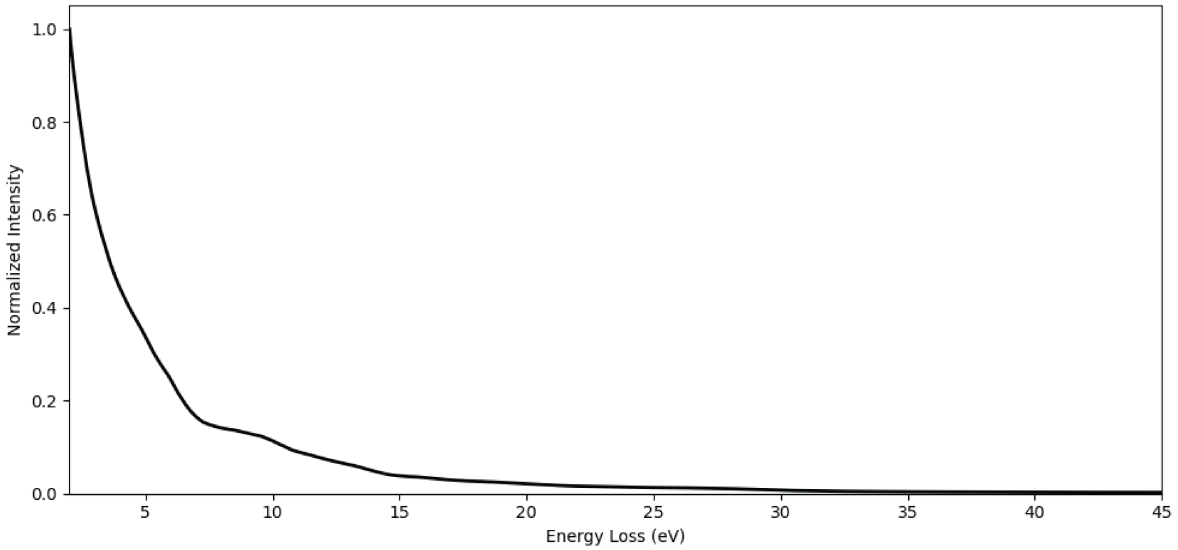

Supplementary Fig. 8 | STEM-EELS spectra over vacuum background regions. The STEM-EELS-averaged spectrum over vacuum depicts the tail of the ZLP without signal from the nanoparticle. Small features due to aloof scattering may be present.

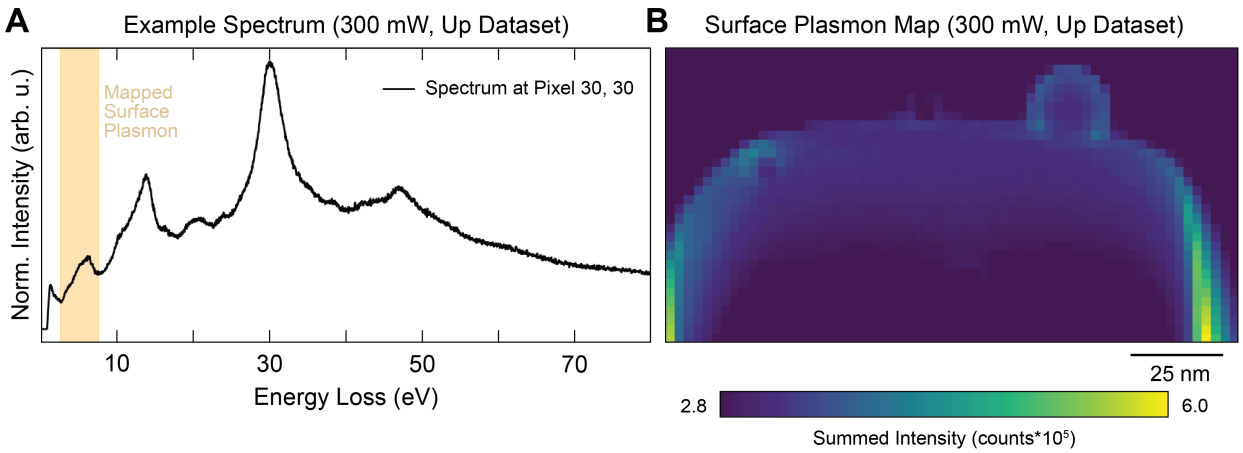

Supplementary Fig. 9 | STEM-EELS map of the $SrTiO_3$ surface plasmon mode. (**A**) An example spectrum at pixel 30, 30 in the 300 mW laser set power (last dataset) depicting the mapped surface plasmon from 3–8 eV. (**B**) The STEM-EELS map of the surface plasmon intensity across the nanoparticle.

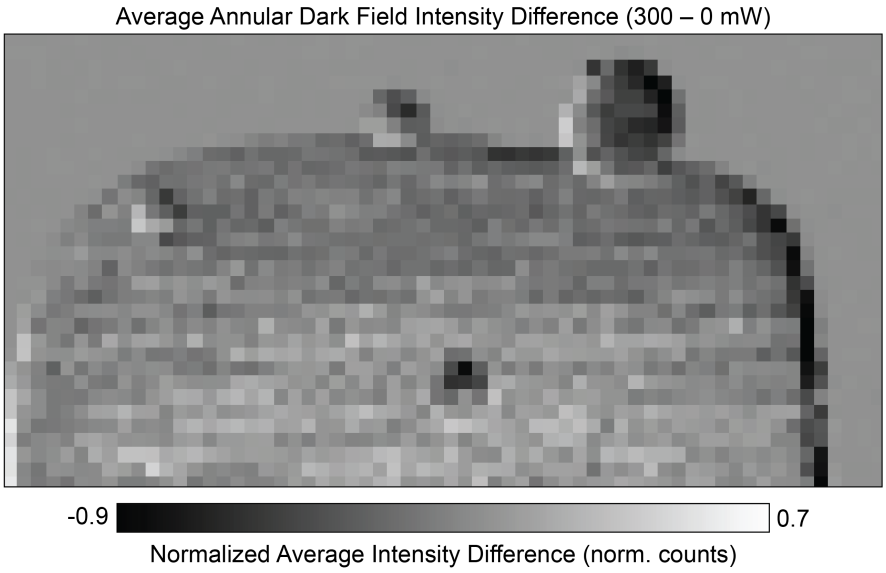

Supplementary Fig. 10 | Photomodulated image drift analysis. The dark field intensity difference between the 300 and 0 mW datasets. The dark-field counts for the two 300 mW and 0 mW datasets were separately normalized and averaged prior to calculating the difference.

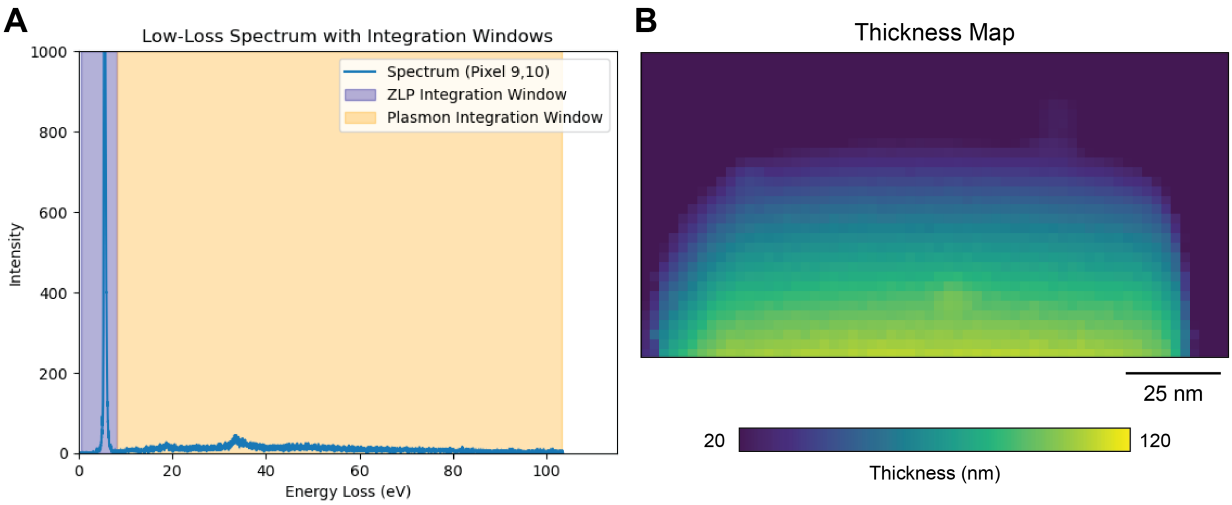

Supplementary Fig. 11 | Nanoparticle thickness map. (**A**) An example low-loss spectrum to depict the analysis windows for the log-ratio thickness mapping method. The spectrum at example pixel 9,10 in the STEM-EELS map is plotted for the studied nanoparticle. (**B**) The thickness map evaluated using STEM-EELS and the log-ratio method. A mean free path of 130 nm was approximated for the 200 kV accelerating voltage.

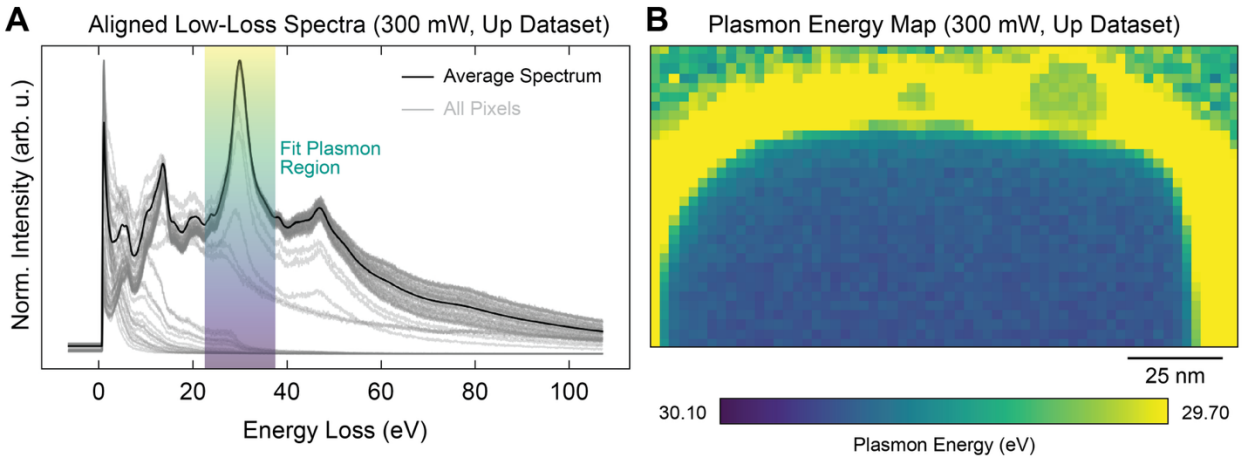

Supplementary Fig. 12 | Photomodulated STEM-EELS averaging and $SrTiO_3$ bulk plasmon map. (**A**) The main plasmon analyzed with center-of-mass fitting. The grey spectra are spectra from all pixels in the STEM-EELS image, and the average spectrum is shown in black. (**B**) A map of the fit plasmon energy across the STEM-EELS map, where only the image pixels over $SrTiO_3$ are quantitative. This result highlights the redshift of the plasmon energy at the nanoparticle's surface.

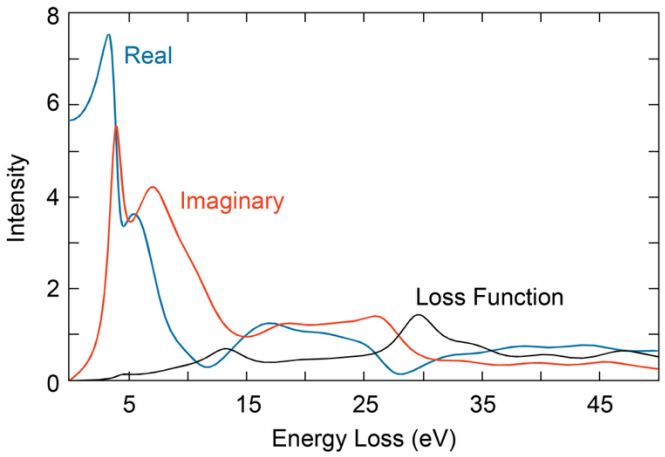

Supplementary Fig. 13 | Calculated dielectric function of $SrTiO_3$. The real and imaginary components of the complex dielectric function of undoped strontium titanate are calculated as a function of energy using TDDFT in turboEELS. The calculated loss function is included for reference.

Supplementary Table 1 | Photomodulated STEM-EELS laser irradiance values and hysteresis cycle. The set laser power and approximate irradiance value in the order used for the hysteresis cycling. Corrected irradiance accounts for photons lost due to fiber coupling, the TEM optical window, and reflections. Approximately 35% of the laser's set beam irradiance illuminates the specimen after losses.

Laser Power (mW)	Irradiance ($mW \cdot cm^{-2}$)	Irradiance Adjusted for Losses ($mW \cdot cm^{-2}$)	Acquisition Order
300	1.5×10^{7}	5.3×10^{6}	1
200	1.0×10^{7}	3.6×10^{6}	2
100	0.51×10^{7}	1.8×10^{6}	3
0	0	0	4
100	0.51×10^{7}	1.8×10^{6}	5
200	1.0×10^{7}	3.6×10^{6}	6
300	1.5×10^{7}	5.3×10^{6}	7

Supplementary Table 2 | Thermal control STEM-EELS temperature values and hysteresis cycle. Set temperature during the STEM-EELS hysteresis cycles in order of acquisition.

Temperature (°C)	Acquisition Order
450	1
250	2
50	3
250	4
450	5

Supplementary Video Legends

Supplementary Video 1 | Spectral projection across all energies of the $SrTiO_3$ low-loss spectrum.

Supplementary Video 2 | Nanoparticle position over all photomodulated measurements.

Supplementary Video 3 | Average power-dependent field map.

Supplementary Video 4 | Average power-dependent carrier map.

Supplementary Video 5 | Average power-dependent temperature map.

Supplementary Video 6 | Average power-dependent dark-field intensity differential map.